Synthesis of Ni-doped ceria nanoparticles and their unusual surface reduction in hydrogen

M. Barreau [a], D. Chen [a], J. Zhang [a], V. Papaefthimiou [a], C. Petit [a], D. Salusso [b], E. Borfecchia [b], S. Turczyniak-Surdacka [c, d], K. Sobczak [c], S. Mauri [e, f], L. Braglia [e], P. Torelli [e], S. Zafeiratos [a, *]

[a] Institut de Chimie et Procédés pour L'Energie, L'Environnement et La Santé, UMR 7515 CNRS-UdS, 25 Rue Becquerel, 67087 Strasbourg, France
[b] Department of Chemistry, INSTM Reference Center and NIS Centers, University of Torino, 10125 Torino, Italy
[c] Faculty of Chemistry, Biological and Chemical Research Centre, University of Warsaw, Żwirki, Wigury 101, 02-089 Warsaw, Poland
[d] Faculty of Chemistry, University of Warsaw, Pasteura 1, 02-093 Warsaw, Poland
[e] IOM CNR Laboratorio TASC, AREA Science Park, Basovizza, Trieste, 34149, Italy
[f] Department of Physics, University of Trieste, Via Valerio 2, Trieste, 34127, Italy

ARTICLE INFO

Keywords:
X-ray absorption spectroscopy
Operando analysis
In situ DRIFT
Square-planar symmetry
NEXAFS

ABSTRACT

This work presents an original approach to preparing pure and Ni-doped CeO_2 nanoparticles (NPs) that can be directly drop-casted on a substrate or calcined to form powders. The reduction of the NPs in H_2 is very different than the one usually anticipated for supported Ni–CeO_2 catalysts. *In situ* soft X-ray absorption and infrared spectroscopies revealed that the reduction of Ce^{4+} into Ce^{3+} in H_2 proceeds via simultaneous oxidation of Ni^{2+} ions into $Ni^{\delta+}$ ($2<\delta<3$). Comparison with reference samples indicates that Ce^{4+} ions reduction is promoted over Ni-doped CeO_2 NPs, whereas that of Ni^{2+} is hindered. Theoretical simulation of Ni L-edge spectra suggested that Ni dopant into ceria is in a square planar four-coordinate environment, in contrast to the familiar octahedral symmetry of bulk nickel oxides. Our results reveal that the surface chemistry of Ni-doped CeO_2 is quite distinct as compared to that of the individual bulk oxides, which potentially can lead to a different performance of this material, notably in catalytic applications.

1. Introduction

Ceria (CeO_2) is a material commonly employed in various catalytic processes, including three-way-catalysis [1,2], NO_x reduction [3], solid oxide cells [4], CO oxidation [5], water-gas-shift reaction [6], CO_2 valorization [7,8] and many more [9]. A key characteristic of CeO_2 is the ease to exchange between Ce^{4+} and Ce^{3+} oxidation states while keeping a rather stable cubic fluorite crystal structure [10]. This property facilitates the creation of oxygen vacancies [11], which can serve both as reservoir of mobile oxygen in bulk and as adsorption sites for reactants on the surface [12]. There are two main strategies to facilitate the reduction of ceria and consequently the creation of vacant sites. The first is to manipulate the size and the surface planes of pure CeO_2 [13,14], and the second is to introduce dopant atoms into the crystal structure [15,16]. For this latter, several elements have been studied, including rare-earth (La, Zr, Gd), platinum group (Ru, Pt), and transition metals (Fe, Ni, Cu, denoted as TM) [6,17,18]. The properties of doped-ceria depend on the size, the valence, and the concentration of the dopant atom. Therefore, the choice of the dopant controls the oxygen storage capacity [19] and the redox behavior of ceria [18].

The synthesis of metal-doped ceria particles is challenging, especially when TM are used as dopants. The use of conventional synthesis methods, such as coprecipitation, sol-gel, or hydrothermal, often leads to a mixture of doped particles and segregated metallic particles [1,20–22]. Among the recent strategies devoted to the synthesis of TM-doped particles [1], the use of organic soft templates has been proven to be effective in obtaining pure-phase particles with small size and size distributions. Briefly, this type of synthesis consists of the self-assembly of isolated cerium and TM in an organic matrix, followed by its removal upon heat treatment. This technique has several advantages: (i) it efficiently impedes the phase separation in single oxides leading to atomic dispersion of

* Corresponding author.
E-mail address: spiros.zafeiratos@unistra.fr (S. Zafeiratos).

the dopant and potentially to single-atom catalysts [23]; (ii) the size of the resulting material is controlled and uniform; (iii) the removal of the organic template can provide high nanoporosity to the finite structure resulting in high-surface-area materials. Particularly, the use of coordination polymers [24] or metal-organic frameworks [15,25,26] turned out to be an efficient strategy for conceiving highly uniform and porous nanostructures. Among the methods proposed, Elias and coworkers prepared monodispersed $M_{0.1}Ce_{0.9}O_{2-x}$ particles (with M = Mn, Fe, Co, Ni, Cu) via pyrolysis of metallic Schiff-base complexes in an oleylamine medium [15]. Although this synthesis method ensures the remarkable production of a wide range of TM-doped ceria catalysts, it suffers from its complexity and low production yields. Recently we reported on the preparation of Ni-doped CeO_2 NPs from Schiff base complexes [25] using an approach with fewer synthesis steps than preceding reports [15]; however, the production yield was still relatively low. Herein, we simplify the synthesis method to produce pure CeO_2 and Ni-doped CeO_2 with small and uniform particle sizes while increasing its yield by a factor of 10. Furthermore, *in situ* surface spectroscopy is employed to examine the reduction of the nanoparticles in 1 bar H_2. It is demonstrated that the reduction of Ni^{2+} in H_2 is hindered, and that of Ce^{4+} is promoted on doped NPs as compared to pure reference samples. Contrary to the generally accepted notion that Ni^{2+} reduction precedes that of Ce^{4+}, we found that Ni^{2+} not only resists reduction but is oxidized further, likely due to electronic interaction with Ce ions. This is a radically different reactivity path than that reported on CeO_2-supported Ni particles [27].

2. Experimental section

2.1. Synthesis of CeO_2 and $Ni_xCe_{1-x}O_2$ NPs

Ni-doped CeO_2 nanoparticles (hereafter named $Ni_xCe_{1-x}O_2$) were prepared from a method recently developed in our group involving the use of Schiff-base metal complexes to produce pure-phase TM-doped ceria nanoparticles [25]. In this four-step method, one step is devoted to the preparation of the Ce^{III}-L, while a two-step reaction is dedicated to the preparation of the heterometallic Ce^{III}—Ni^{II}-L (where L = N,N′-bis(3-methoxysalicylidene)-propylene-1,3-diamine). Finally, the last step consists in mixing the metallic complexes in oleylamine media and followed by pyrolysis at 180 °C under an inert atmosphere [25]. In the present paper, this method has been simplified in several ways: (i) the number of steps has been lowered to three, using only monometallic complexes for the synthesis (Ce^{III}-L and Ni^{II}-L). In other terms, the bimetallic complex preparation has been discarded since we observed that it is not a prerequisite for the preparation of monodisperse Ni-doped CeO_2 nanoparticles; (ii) the synthesis yield was improved by a factor of 10 while lowering the solvent/reactant ratio, allowing to produce more catalyst (from 50 to 100 mg to around 1 g with the new method) without using excessive amounts of solvent; (iii) after pyrolysis of the metallic Schiff-base complexes under oleylamine medium, the NPs were extracted using methanol instead of ethanol, which has been found to be more efficient to precipitate the NPs.

2.1.1. Preparation of Ce(III)-L

In a solution of 200 ml of methanol were added 3 g of 2-hydroxy-3-methoxybenzaldehyde (20 mmol), 0.7 g of 1,3-diaminopropane (10 mmol), and 4.06 g of $Ce(NO_3)_2.6H_2O$ (10 mmol), giving a yellow precipitate immediately. The yellow suspension was stirred at reflux for 3h before cooling down to room temperature. The crude product was filtered through a frit, washed several times with cold EtOH, and dried under vacuum to give Ce^{III}-L as a yellow powder.

2.1.2. Preparation of Ni (II)-L

In a three-necked flask were mixed 8 g of 2-hydroxy-3-methoxybenzaldehyde (52.6 mmol), 2.1 g of 1,3-diaminopropane (30 mmol), and 6.66 g $Ni(OCOCH_3)_2.4H_2O$ (27 mmol) in a solution of 100 ml of methanol. The green solution was refluxed at 80 °C for 4 h before cooling down to room temperature. The green crystals obtained after reducing the volume of the solution to 20 ml were then filtered and washed several times with methanol.

2.1.3. Preparation of $Ni_xCe_{1-x}O_2$ nanoparticles

The $Ni_xCe_{1-x}O_2$ nanoparticles were prepared by mixing 5.1 of Ce^{III}-L and 1.5 g of Ni^{II}-L in 200 ml of oleylamine. The mixture was refluxed at 180 °C under argon for 4 h, and the remaining dark brown product was isolated by centrifugation. Around 450 ml of methanol were added to the solution leading to the precipitation of the nanoparticles. Consequently, the brown flocculent was isolated by centrifugation. After recuperation of the NPs by centrifugation (4400 rpm for 10 min), the NPs were calcined under air at 450 °C for 1 h, leading to approximately 1 g of powder. A similar protocol was used for the preparation of undoped CeO_2 particles by pyrolysis of only Ce^{III}-L in oleylamine.

2.2. Characterization techniques

2.2.1. Standard characterization

Ex situ X-ray diffraction (XRD) patterns of the calcined samples were recorded on a Bruker D8 advance diffractometer operating at 40 kV and 40 mA using Cu Kα radiation (λ = 1.5418 Å). XRD patterns were recorded from 20 to 80° at a scan rate of 0.032° s^{-1}. The resulting patterns were processed using DIFFRAC.EVA for the crystallite size calculation according to the line broadening of the most intense reflection (i.e. the (111) plan for the fluorite-type CeO_2 phase) using the Scherrer equation, while the FullProf software [28] was used for the Rietveld refinement and the determination of the lattice parameters. Raman spectra were measured using a micro-Raman spectrometer (Horiba LabRam Aramis). A 10 × objective was used to focus the excitation laser with an excitation wavelength of 532 nm, giving approximately a 2.6 μm wide spot with a laser power of less than 1 mW in order to avoid damaging the sample. Temperature-Programmed Reduction of the catalysts by hydrogen (H_2-TPR) was carried out in an AutoChem II apparatus (Micromeritics) incorporating a thermal conductivity detector (TCD). The profiles were obtained after loading 50 mg of sample in a U-shaped fixed bed reactor and heating at 950 °C under 20 ml/min of 10% H_2/Ar with a 10 °C min^{-1} heating rate. Elemental analysis of the Ni-doped CeO_2 material was carried out by Inductively Coupled Plasma Optical Emission Spectroscopy (ICP-OES, Varian 720 ES) after the dissolution of the powdered sample in acidic medium (HNO_3) followed by filtration of residual particles.

The TEM investigations were carried out using an FEI Talos F200X microscope operating at 200 kV. Observations were performed in scanning transmission electron microscopy (STEM) mode using high-angle annular dark-field (HAADF) imaging. Energy-dispersive X-ray spectroscopy (EDX) using a Super-X system with four silicon drift detectors (SDDs) was applied to the detection of differences in local chemical composition.

2.2.2. In situ infrared experiments

In situ Diffuse Reflectance Infrared Fourier Transform Spectroscopy (DRIFTS) was used to investigate the behavior of different functional groups characterizing the samples under air or H_2 while heating. The experiments were performed on a Bruker Vertex 70

FTIR spectrometer equipped with a Praying Mantis diffuse reflectance accessory and a tailor-made reaction cell with ZnSe windows. A cold trap was placed at the inlet of the reaction cell in order to remove water traces from the gas feed. Prior to the tests, the powder samples were grounded with a mortar and diluted with KBr in order to avoid signal saturation (10 wt% in KBr). A background (64 scans, 4 cm^{-1}) was acquired by placing pure KBr in the reaction cell. Then, around 120 mg of diluted sample were loaded into the cup and deposited in the center of the reaction cell for the analysis. The sample was first subjected to an oxidative treatment under 10 ml/min of synthetic air to 400 °C with a 10 °C min^{-1} heating rate for 30 min. After cooling down to 120 °C, a reducing treatment was subsequently realized under 10 ml/min of H_2 at 400 °C for 30 min. Spectra were recorded continuously during the treatments via the execution of a macro with an accumulation of 32 scans at a resolution of 4 cm^{-1}.

2.2.3. In situ sXAS experiments

The soft X-ray absorption spectroscopy (sXAS) experiments were performed at the APE-HE beamline of the Elettra synchrotron radiation facility (Trieste, Italy), exploiting a dedicated setup based on a reaction cell with Si_3N_4 membranes, as described in detail elsewhere [29]. The sXAS signal was detected in TEY mode by probing the drain current from the sample with a picoammeter. The catalyst powder was loaded in the *in situ* cell, installed in the APE-HE instrument, and interfaced with gas delivery and temperature control systems. Gas flows were monitored by calibrated mass flow controllers. All reported experiments were performed at a gas pressure of 1 bar. The sample was initially pretreated in 10% O_2/He mixture at 340 °C for about 30 min and then cooled to room temperature under He gas flow. Then the gas atmosphere was switched to 10% H_2/He mixture, and the temperature was raised at a rate of 2.5 °C/min up to 360 °C, while *in situ* sXAS Ni L- and Ce M-edges spectra were recorded at selected temperatures. Finally, the sample remained for about 30 min at the maximum annealing temperature before cooling down in H_2/He. Spectra analysis was performed using the CasaXPS vs. 2.3.23 software. The background subtraction was done using a spline-linear function.

The shape of the Ce $M_{5,4}$ edge is distinguishably different between the Ce^{3+} and Ce^{4+} oxidation states; therefore, the differences in the oxidation state can be easily detected based on the overall peak shape. In particular, the Ce M_5-edge spectra were fitted by a linear combination of standard reference curves of Ce^{4+} and Ce^{3+} species recorded at the same spectrometer over a 10%Ni–CeO_2 sample prepared by the impregnation method. The Ce M_5-edge corresponding to Ce^{4+} was recorded after O_2 treatment at 360 °C, while the Ce^{3+} one after a long-time reduction in H_2 at 350 °C. Fitting was performed after linear background subtraction, while the full width at the half maximum and the energy difference among the two reference peaks were fixed. The reference peaks were allowed to vary until the difference between their sum and the experimental spectra (residual standard deviation, STD) was minimized (typical STD between 0.005 and 0.010).

In the case of Ni $L_{3,2}$ edge, the modifications between the various nickel oxidation states are less evident in the peak shape, and therefore, it is important to define the position of the peak. In order to be able to exclude artifacts in the peak position between different samples and conditions, we used the position of the most prominent feature of the Ce M_5-edge as an internal reference for all the samples and conditions. The position of this peak was fixed at 884 eV, and the position of the Ni L-edge was calculated according to this value. All the sXAS spectra shown in this paper have been calibrated using this method. The position of the reference Ni (metallic) and NiO peaks was collected *in situ* over a reference sample composed of 10%Ni on CeO_2, after reducing and oxidizing treatments.

2.2.4. Charge-transfer multiplet calculations

The Ni $L_{3,2}$-edge was simulated using the charge-transfer multiplet (CTM) approach using the CTM4XAS 5.23 program [30]. We attempted to fit the experimental Ni $L_{3,2}$-edge spectra with both octahedral and tetrahedral symmetries; however, only the latter symmetry gave theoretical curves in resemblance with the experimental ones. The crystal field value (10Dq) and the charge transfer energy value (Δ) were the main parameters adjusted in the simulation to obtain the best accordance with the experimental spectra. Other simulation parameters were as follows: (i) for Ni^{2+} slater integrals (F_{dd}, F_{pd}, G_{pd}) = 1, spin-orbit spitting parameter SO = 0.99, optical parameters Dt = 0.1, Ds = 0.05eV, core hole potential U_{pd} and the 3d-3d repulsion energy U_{dd}=0, U_{pd}nbsp;= −1.8, and the hopping parameters $e_g$nbsp;= 2 eV and t_{2g} = 1 eV, Temperature 600K; (ii) for $Ni^{\delta+}$, (F_{dd}, F_{pd}, G_{pd}) = 1, SO = 0.97, Dt = 0.13, Ds = 0.05eV, U_{dd}=0, U_{pd}nbsp;= −0.1, $e_g$nbsp;= 1 eV and t_{2g} = 1.5 eV, Temperature 600K.

3. Results and discussion

3.1. Synthesis and ex situ characterization

Ni-doped CeO_2 NPs (hereafter abbreviated as $Ni_xCe_{1-x}O_2$ with x = 0.036, determined by ICP-OES) were prepared from Schiff-base metal complexes as detailed in the experimental part. Briefly, the method involves the preparation of the monometallic Ce^{III}-L and Ni^{II}-L complexes followed by their pyrolysis at 180 °C in an inert atmosphere under oleylamine media. After cooling down to room temperature, the resulting nanoparticles are obtained by extraction with methanol and finally dispersed in hexane solution or calcined at 450 °C to form a powder (Fig. 1). A similar protocol was used for the preparation of undoped CeO_2 particles (hereafter abbreviated as CeO_2). The production yield was around 1g of NPs, which is around 10 higher than that of previous reports (50–100 mg) [25].

The XRD patterns of calcined nanoparticles (Fig. S1a) are characteristic of the cubic fluorite phase (JCPDS 34–0394). The absence of any Ni-containing crystal phases discards the presence of segregated Ni particles and confirms the high dispersion of Ni at $Ni_xCe_{1-x}O_2$. The analysis of the XRD results, presented in Table 1, shows similar crystallite sizes of the two NPs types (ca. 6.7 nm). The lattice parameters of both samples are lower than the theoretical value of bulk ceria (5.411 Å), which can be attributed to reduced surface relaxation in small nanoparticles [22]. A slight increase (0.13 ± 0.01%) of the $Ni_xCe_{1-x}O_2$ lattice parameter as compared to CeO_2 (Table 1) can be indicative of the Ni occupation sites in the ceria lattice. In particular, Ni ions may substitute lattice Ce^{4+} (substitutional sites) or alternatively occupy interstitial lattice positions (interstitial sites), while they may easily exchange between the two sites, depending on the conditions (e.g. temperature) [31,32]. Although in both cases, nickel is stabilized as Ni^{2+} [31], the ceria lattice parameters are distinct. Substitution of Ce^{4+} with the smaller Ni^{2+} cations (83 p.m. for Ni^{2+} vs. 101 p.m. for Ce^{4+}) would lead to lattice contraction, while lattice expansion is expected for Ni impurities at interstitial ceria sites [32]. The increase of the lattice parameter in Table 1 not only confirms the successful doping of Ni atoms but is also compatible with Ni^{2+} at interstitial ceria sites [32].

According to the theoretical study of Chafi et al. [33], when a nickel atom is located at interstitial sites of the cubic fluorite ceria lattice, an increase of the ceria lattice parameter is expected. This is due to the large repulsion between Ce atoms around the Ni-dopant, causing expansion of the CeO_2 lattice. As Ni concentration

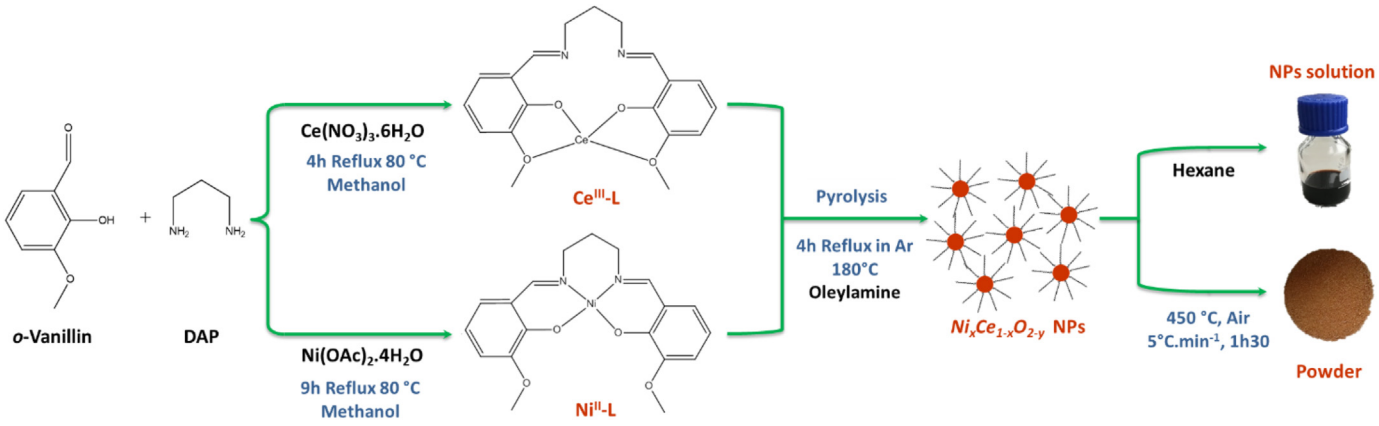

Fig. 1. Illustration of the $Ni_{0.1}CeO_x$ NPs preparation method. For the CeO_2 NPs synthesis, a similar protocol was used, with only Ce^{III}-L Schiff-base complexes.

Table 1
Structural and textural parameters of calcined samples.

Catalyst	Crystallite size[a] (nm)	Lattice parameter[b] (±0.0005 Å)	Volume cell[b] (±0.03 Å^3)
CeO_2	6.8	5.4082	158.18
$Ni_xCe_{1-x}O_2$	6.6	5.4153	158.81

[a] Crystallite size estimated from the Scherrer's equation applied to the most intense (111) diffraction peak.
[b] Data obtained from Rietveld refinement using FullProf software.

increases, the insertion becomes more exothermic, allowing easier insertion of Ni atoms [33]. Of course, one should also mention here that the enhanced reducibility of $Ni_xCe_{1-x}O_2$ can be an additional cause of lattice expansion. Since the size of Ce^{3+} is larger than that of Ce^{4+} (rCe^{3+} = 1.143 Å, rCe^{4+} = 0.970 Å; both ions are 8-fold coordinated), reduction of ceria would also induce lattice expansion in order to retrieve the strain induced by the Ce^{3+} ions [34]. Although we cannot totally exclude the enhanced reducibility of $Ni_xCe_{1-x}O_2$ as the cause of the observed lattice expansion, we assume that this mechanism is quite unlikely since the XRD measurements were performed over calcined samples.

The Raman spectrum of ceria is dominated by a sharp peak attributed to the triply degenerate oxygen breathing mode of F2g symmetry, characteristic of cubic fluorite structure. As shown in Fig. S1b, in the case of CeO_2, the F2g peak is located at 464 cm^{-1}, while for $Ni_xCe_{1-x}O_2$, it shifts at 460 cm^{-1} and becomes broader. The shift of the F2g Raman peak to lower wavenumbers indicates an expansion of the average fluorine lattice parameter of ceria due to Ni doping, in full agreement with the XRD results [10,35,36]. In addition, new bands appear at 228, 558, and 625 cm^{-1} for the $Ni_xCe_{1-x}O_2$ sample. These peaks are attributed to the D band defects and the creation of O vacancies due to nickel solubility [37,38].

Fig. 2a and b show representative TEM and HR-TEM images combined with selected area electron diffraction (SAED) patterns. The TEM images of the calcined sample show aggregation of small and uniform nanoparticles. The particle size distribution histogram inserted in Fig. 2a, indicates a mean CeO_2 particle size around 7.7 nm, in fair agreement with the crystalline sizes found by XRD (6.8 nm, see Table 1). The HR-TEM image combined with the SAED pattern in Fig. 2a shows distinct diffraction spots and lattice fringes spacing corresponding to the planes of CeO_2 NPs. The microscopy analysis of $Ni_xCe_{1-x}O_2$ (Fig. 2b) shows similar particle morphology to CeO_2, but the mean particle size is somewhat smaller (5.5 nm). The diffraction patterns correspond to that of ceria; however in the EDX mapping (Fig. 2d and Fig. S2), the presence of nickel is evident and is quantified to 3.5% Ni atomic ratio, corroborating the $Ni_{0.036}Ce_{0.964}O_2$ stoichiometry determined separately by inductively coupled plasma atomic emission spectroscopy (ICP-OES). The Ni and Ce mappings indicate a rather homogenous mixture of the two elements, although some areas richer in Ni are visible (see also Fig. S2 showing higher EDX analysis area). Interesting structural information comes from the comparison of the high-resolution images and diffraction patterns between areas with high and lower nickel signals (Fig. 2c). From this, it is shown that Ni significantly increases the lattice planes of the ceria crystalline phase, corroborating the lattice parameter difference observed in XRD and confirming the integration of nickel in the ceria lattice. Consequently, diffraction and microscopy results of $Ni_xCe_{1-x}O_2$ NPs confirm Ni incorporation into CeO_2 lattice [39].

The reducibility in H_2 was initially investigated by H_2-TPR (Fig. S3). The H_2-TPR profile of CeO_2 exhibits two broad peaks with a maximum of around 500 °C and 850 °C, typically assigned to the reduction of the surface and bulk Ce^{4+} ions, respectively [40,41]. In the case of $Ni_xCe_{1-x}O_2$, an additional peak at 310 °C is evident, which was previously linked to NiO reduction [42]. However, the high H_2 uptake in our case (estimated to be 644 µmol/g), is incompatible with the low nickel amount of $Ni_xCe_{1-x}O_2$ NPs (x = 0.036), which would theoretically lead to three times lower H_2 consumption than the one observed (see Fig. S3). The origin of this peak is probably due to Ce^{4+} reduction, as will be explained below on the basis of *in situ* sXAS.

3.2. *In situ* DRIFTS analysis

The reduction of preoxidized CeO_2 and $Ni_xCe_{1-x}O_2$ samples was followed by *in situ* DRIFTS. Fig. 3 displays 2D maps recorded during heating in pure H_2, while DRIFT spectra are shown in Fig. S4. The stretching vibrations of OH groups can be followed in the 3900-3550 cm^{-1} region, while the 2250-1950 cm^{-1} region gives information about the cerium oxidation state. The H_2 treatment induces progressive dehydroxylation, characterized by several negative peaks in the 3900–3550 cm^{-1} region. An intense band is observed for both samples at 3658 cm^{-1} together with features in the 1800–1100 cm^{-1} region (not shown), assigned to desorption of

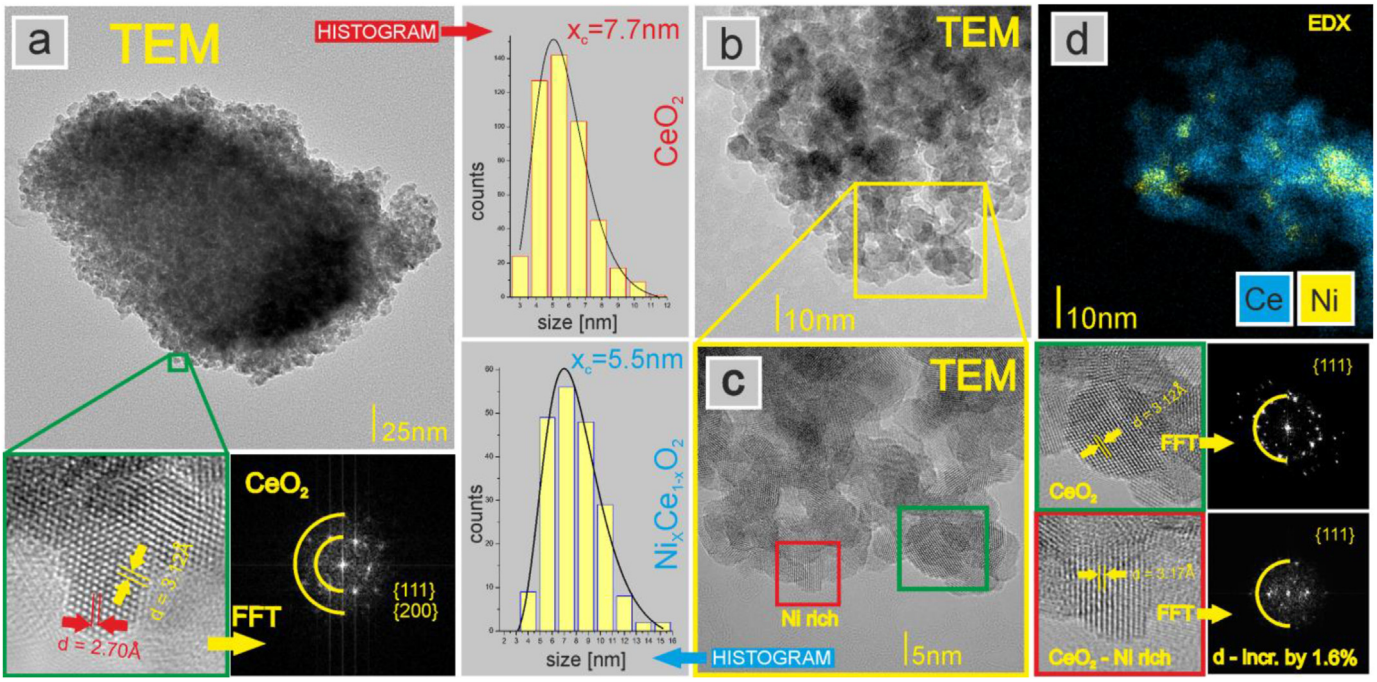

Fig. 2. HAADF-STEM images of calcined (a) CeO_2 and (b,c) $Ni_xCe_{1-x}O_2$ NPs samples. The particle size distribution histogram, HR images, and selected SAED patterns are inserted in the two figures. (d) EDX mapping of $Ni_xCe_{1-x}O_2$ sample indicating mixing of Ni and Ce elements.

bicarbonate compounds, probably remaining on the sample surface after calcination. Starting from 200 °C two additional peaks at 3709 cm^{-1} (terminal OH groups-Type I) and 3685 cm^{-1} (bridging OH groups-Type II) [43–45], are observed on $Ni_xCe_{1-x}O_2$. Therefore, $Ni_xCe_{1-x}O_2$ is differentiated from CeO_2 by desorption of poly-coordinated OH groups during heating in H_2. According to the literature [46], type I OH groups have a higher propensity to dissociate as OH^- anions, causing the creation of charge deficiency on the coordinated cerium atom upon their removal. Interestingly, at 300 °C a broad band at 2117 cm^{-1} appeared on $Ni_xCe_{1-x}O_2$, the intensity of which increases with temperature. This band has been attributed to the forbidden $^2F_{5/2} \rightarrow {}^2F_{7/2}$ electronic transition of Ce^{3+} [47]. This peak is much less evident for CeO_2 and appears only at the maximum annealing temperature (400 °C). According to these results, the reduction of Ce^{4+} to Ce^{3+} over $Ni_xCe_{1-x}O_2$ takes place between 300 and 400 °C simultaneously with surface dehydroxylation.

3.3. *In situ* sXAS analysis

It is important to note that the DRIFTS bands associated with Ce^{3+} ions come from a sampling depth of a few μm. The nickel and cerium oxidation states at the outer 5 nm [48] of the NPs are examined by *in situ* sXAS in 1 bar 10% H_2/He. Characteristic Ni $L_{3,2}$-edge spectra of $Ni_xCe_{1-x}O_2$ upon annealing in H_2 are shown in Fig. 4a. The position of the Ni $L_{3,2}$-edge (centroid of the peak) and its shape (multiplet structure) are sensitive to the nickel chemical environment (i.e. oxidation state, coordination symmetry, and interaction with ligand ions). In general, the Ni L_3-edge centroid shifts to higher energy for higher nickel oxidation [49,50], while the peak features around 855 and 872 eV are sensitive to Ni interaction with the ligand ion (O^{2-}) (e.g. transformation of nickel oxide to hydroxide) [51]. The Ni $L_{3,2}$-edge of calcined $Ni_xCe_{1-x}O_2$ (50 °C in Fig. 4a) has the same centroid position with reference bulk NiO (852.8 eV) but quite a different edge shape. This indicates bivalent nickel ions (Ni^{2+}) but in a different chemical environment as compared to the standard octahedral NiO. The Ni $L_{3,2}$-edge is stable up to 230 °C, but above this temperature, the peak becomes broader, and two distinct Ni L_3 features appear at 852.6 and 853.4 eV. The Ni $L_{3,2}$-edge measured above 230 °C does not resemble any of the standard nickel oxide or hydroxide spectra [51], while its complex peak shape suggests the possible overlapping of two, or more, nickel chemical states. Attempts to simulate the Ni $L_{3,2}$-edge by the linear combination of Ni, NiO, and oxidized $Ni_xCe_{1-x}O_2$ reference peaks were unsuccessful. The accuracy of the fitting was improved when one of the reference peaks ($Ni_xCe_{1-x}O_2$, up to 310 °C, and metallic Ni^0, from 325 to 360 °C) is combined with a spectrum composed by 4 Gaussian/Lorentzian peaks (Fig. 4a and Figs. S5 and S6) and shifted to a higher energy than Ni^{2+} by 0.6 eV. Since the multiplet structure of this spectrum does not resemble the trivalent Ni^{3+} ions [51,52], we attribute it to a nickel oxidation state between 2 and 3, denoted as δ ($Ni^{\delta+}$ with $2< \delta<3$). The appearance of $Ni^{\delta+}$ is a remarkable observation, which, contrary to the common consensus, indicates oxidation of Ni ions in 1 bar H_2. Notably, when the sample is cooled down in H_2 the Ni $L_{3,2}$-edge is modified, and Ni^{2+} reappears (Fig. S6), suggesting that the reported behavior can be observed only *in situ* and it is elusive to post-treatment analysis.

The Ce M_5-edge of the oxidized $Ni_xCe_{1-x}O_2$ corresponds to the Ce^{4+} state (Fig. 4b), while starting from 265 °C, the absorption edge is modified due to the formation of Ce^{3+} as indicated by the linear peak fitting analysis of Ce M_5-edge depicted in Fig. S7. Partial reduction of ceria is, of course, expected upon annealing in H_2; however, the ease of ceria reduction (e.g. the amount of Ce^{3+} species and the temperature they appear) in Ni-doped samples as compared to standard nanosized ceria with similar physico-structural properties is of major interest for the applications and will be analyzed below.

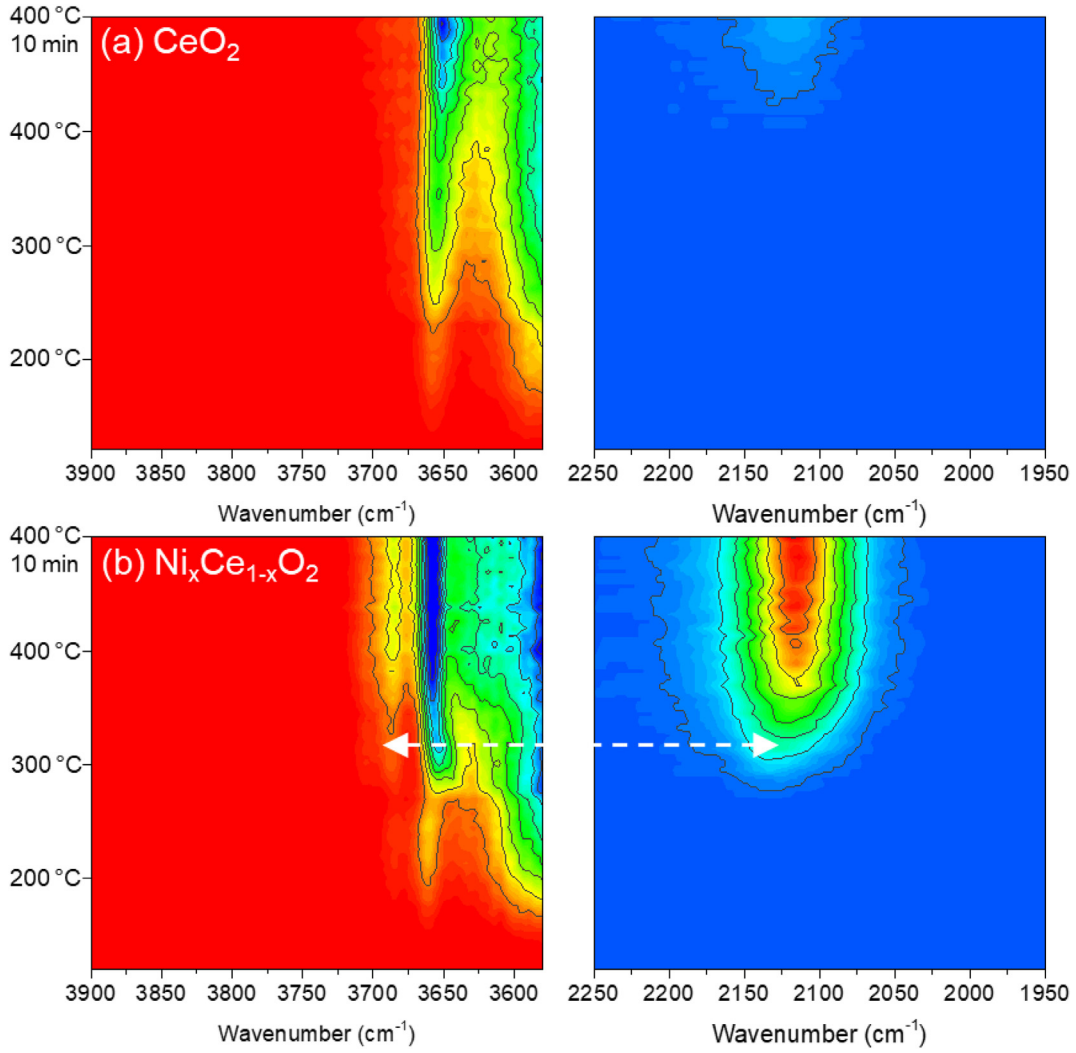

Fig. 3. 2D mapping of the DRIFTS spectra recorded in 1 bar H_2 during heat treatment up to 400 °C after background subtraction and applying Kubelka-Munk equation for a) CeO_2 and b) $Ni_xCe_{1-x}O_2$. In the 3900-3580 cm^{-1} range (left panels), the color scale goes from $f(r_\infty) = 0$ (red) to negative values (blue). In the 2250-1950 cm^{-1} range (right panels), the color scale goes from $f(r_\infty) = 0$ (blue) to positive values (red).

3.4. Charge-transfer multiplet calculations of Ni $L_{3,2}$-edge

The formation of Ni^{2+} ions in Ni-doped ceria is supported by previous experimental findings [31,32], and first-principle calculations [53,54]. To get more insights into the local electronic structure and the chemical bonding of Ni ions in $Ni_xCe_{1-x}O_2$ NPs, we perform charge-transfer multiplet (CTM) calculations of the Ni $L_{3,2}$-edge using the CTM4XAS 5.23 software [30,55]. Calculated and experimental Ni $L_{3,2}$-edges of Ni^{2+} and $Ni^{\delta+}$ states are shown in Fig. 5. Please note that CTM calculations describe quite well the experimental atomic multiple splitting and therefore, the Ni L-edge shape; however, they cannot reproduce with accuracy the position of the Ni L-edge [56]. Therefore in Fig. 5 the centroid position of the theoretically simulated Ni L-edge is aligned to the centroid of the experimental peak. As shown in Fig. 5 the experimental spectra are accurately simulated assuming Ni^{2+} ions in square planar D_{4h} coordination symmetry (for brevity, $Ni^{2+}[D_{4h}]$). Attempts to reproduce them by octahedrally (O_h) coordinated Ni^{2+} ions failed since $Ni^{2+}[O_h]$ ions have a characteristic double-peak L_2-edge [57,58], very different from the spectra in Fig. 4a.

The $Ni^{2+}[D_{4h}]$ geometry has been verified for Ni–S compounds [49,57] and salen complexes [59] by sXAS. However, as far as we are aware, this is the first time that $Ni^{2+}[D_{4h}]$ sites have been observed in the case of doped oxide particles. This structure is in sharp contrast with Ni ions coordinated in the bulk NiO, which is known to crystallize in the O_h symmetry. Our experiments confirm the earlier theoretical studies predicted that when Ni substitutes lattice Ce atoms, instead of the conventional octahedral coordination, it is coordinated by four O atoms in a square-planar environment [32,54,60]. For example, in the case of the CeO_2(111) surface, two lattice oxygen atoms that were initially three-fold coordinated with Ce ions become two-fold coordinated Ni [60]. Similar predictions regarding four-fold coordinated Ni were also reported for Ni ions occupying interstitial lattice positions, at least for low Ni dopant concentrations [33]. In this case, Ni atoms are located at the center of the cube formed by the eight oxygen atoms in the fluorite unit cell [33].

Apart from the local geometry, the analysis of the 10Dq and Δ parameters, defined in the CTM calculations, provides information about the nickel-ligand (Ni–O) interactions. In particular, the 10Dq term increases when the Ni and O ions come closer, while an increased Δ parameter denotes weaker Ni–O interactions [61]. The simulation of the $Ni^{\delta+}$ spectrum needs higher 10Dq and lower Δ values (10Dq = 0.9 and Δ = 3) as compared to the Ni^{2+} (10Dq = 0.5

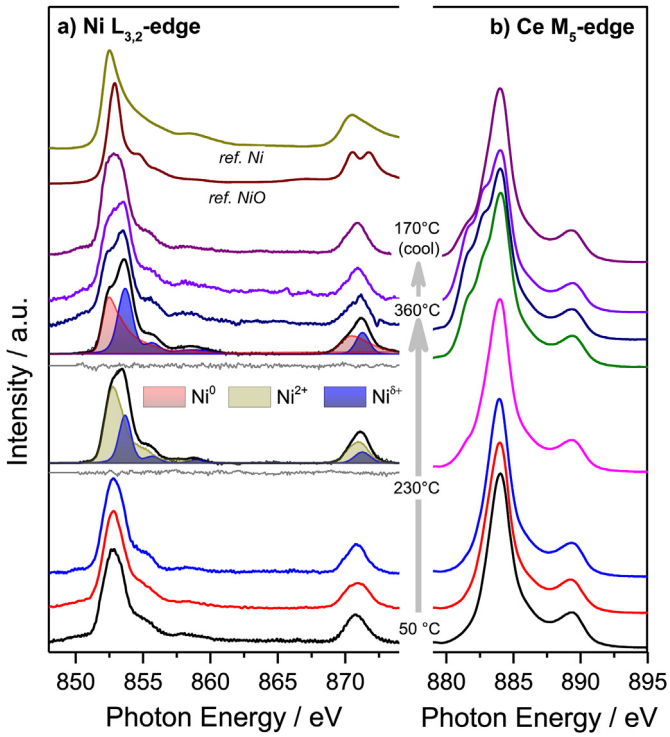

Fig. 4. (a) Ni $L_{3,2}$-edge sXAS spectra of pre-oxidized $Ni_xCe_{1-x}O_2$ NPs upon annealing in 1 bar 10% H_2/He mixture. Two characteristic cases of Ni $L_{3,2}$-edge fitting, as well as peaks of metallic and NiO reference samples, are included. (b) Ce M_5-edge sXAS recorded at the same conditions as described in (a).

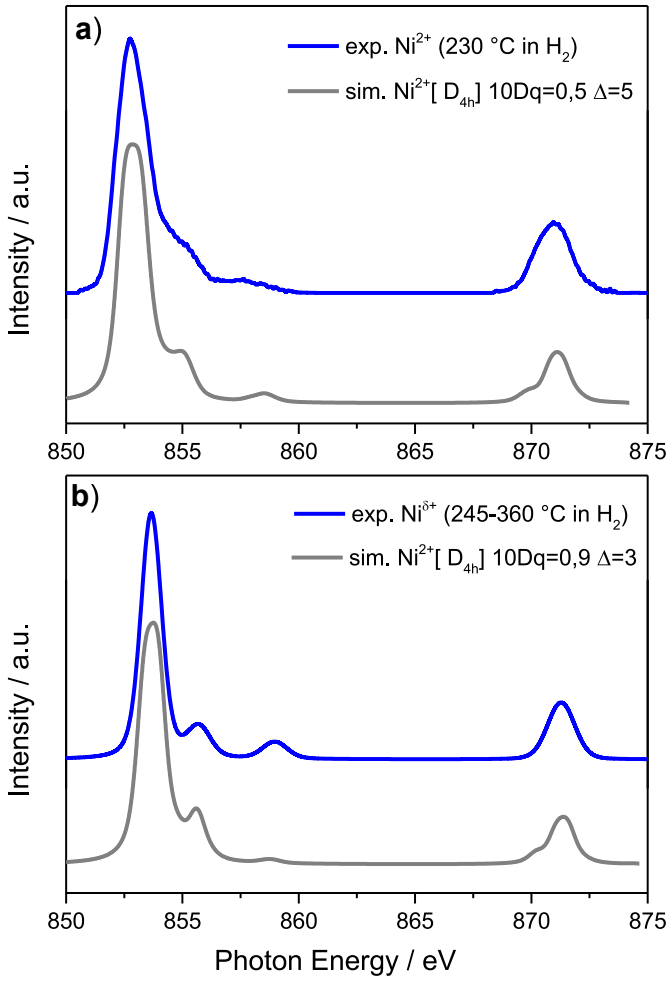

Fig. 5. *In situ* Ni $L_{3,2}$-edge sXAS spectra (blue lines) of (**a**) the Ni^{2+} state recorded at 230 °C and (**b**) the $Ni^{\delta+}$ state composed of 4 G/L peaks and used to fit the experimental spectra between 245 and 360 °C in 1 bar 10% H_2/He. The theoretically simulated Ni $L_{3,2}$-edge (gray lines) for square-planar (D_{4h}) coordinated Ni^{2+} ions and the corresponding 10Dq and Δ values used in the simulations are included in the figure.

and $\Delta = 5$) as shown in Fig. 5 and specified in experimental part. These differences indicate smaller square size, and larger attractive interactions, between $Ni^{\delta+}$ and O^{2-} ions as compared to the $Ni^{2+}$of the fully oxidized sample. This means an increasing covalent character of the $Ni^{\delta+}$-O^{2-}, which can explain the stability of these species under severe reducing conditions.

3.5. The evolution of nickel and ceria oxidation states as compared to reference samples

The evolution of Ni^0 and $Ni^{\delta+}$ states as a function of temperature, as derived from the Ni-$L_{3,2}$ edge deconvolution, is shown in Fig. 6a. The results collected over the NiO powder sample are included for comparison. The amount of $Ni^{\delta+}$ enhances continuously at the expense of Ni^{2+}, up to the maximum annealing temperature. Metallic Ni^0 appears rather abruptly around 330 °C, which is 130 °C higher than the NiO reference. One should note here that the distributions of nickel and cerium states shown in Fig. 6 represent their contribution to the sXAS spectrum, as this is given by the peak fitting analysis. Eventual differences in the photoabsorption cross section (PCS) between different oxidation states are not considered since these values are practically unknown. However, metallic nickel is expected to have lower PCS than the oxidized one due to the lower number of empty 3d band states. Therefore, the Ni^0 concentration shown in Fig. 6a is most probably underestimated.

The results of linear peak fit analysis of the Ce M_5-edges shown in Fig. 6b reveal a sharp increase of Ce^{3+} contribution above 270 °C. When the CeO_2 NPs are exposed to the same conditions (the Ce M_5-edges are shown in Fig. S8), they are less reduced (Fig. 4b). This result can be used to associate the lower temperature peaks of the $Ni_xCe_{1-x}O_2$ NPs found in the TPR analysis (Fig. S3) with the ease of ceria reduction in this sample. Since Ni-doped and pure ceria nanoparticles have very similar size distribution (Fig. 2), one can exclude that their reducibility is affected by differences in their size. Therefore, the promotion effect of Ni-dopant remains the most plausible explanation of the improved ceria reducibility by H_2.

Very interesting findings regarding the mechanism of $Ni_xCe_{1-x}O_2$ reduction emerge by comparison of Fig. 6a and b. The first remarkable observation is that Ce^{4+} reduction is not preceded by the reduction of Ni^{2+}, as commonly assumed for supported nickel particles. On the contrary, Ni^{2+} is oxidized further to $Ni^{\delta+}$. Metallic Ni^0 is observed 70 °C higher than in Ce^{3+}, yet it coexists with a significant amount of $Ni^{\delta+}$ species. In previous studies of the nickel-ceria system [62,63], it was proposed that electrons can transfer from Ce^{4+} towards nickel, generating Ni^{2+} and Ce^{3+}. Although, in our case, the geometry of the system is different (diluted, instead of supported, nickel ions), one can propose that a similar mechanism also takes place for $Ni_xCe_{1-x}O_2$, where Ce^{4+} is transformed to Ce^{3+} by transferring electrons toward Ni^{2+} to form $Ni^{\delta+}$. The charge exchange between $Ni^{\delta+}/Ni^{2+}$ and Ce^{4+}/Ce^{3+} redox couple can be the reason for the enhanced Ce^{4+} reducibility on $Ni_xCe_{1-x}O_2$ as compared to the CeO_2 sample, at least at the initial stage of reduction. When metallic Ni^0 is formed, Ce^{4+} reduction can take place via the classical reduction mechanism related to adsorption

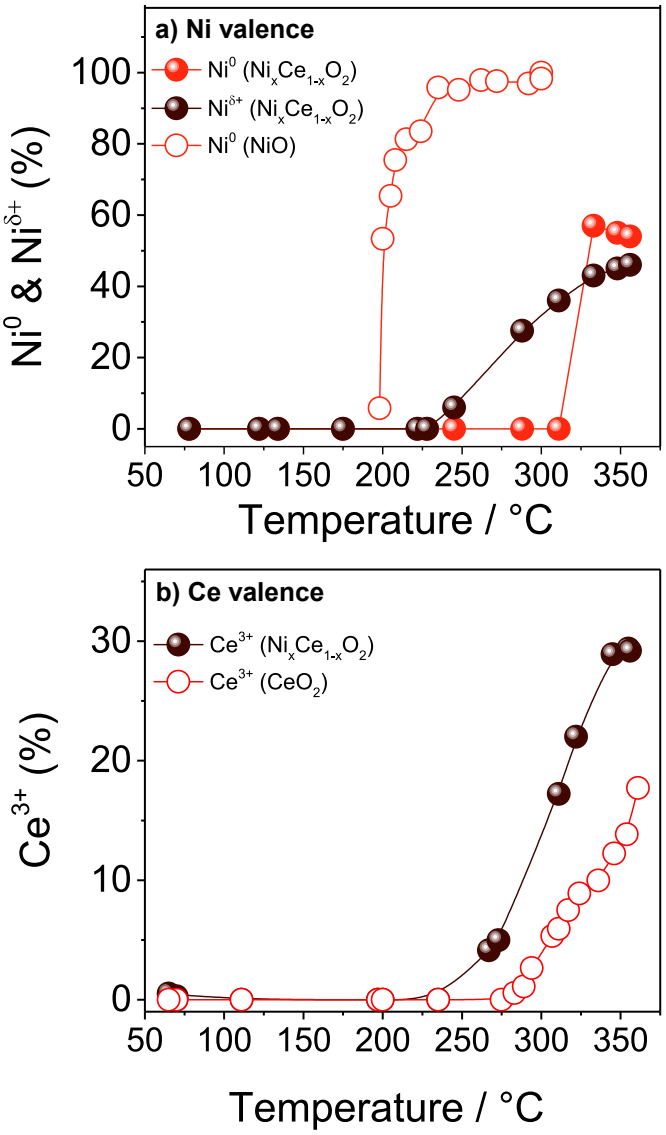

Fig. 6. (a) Evolution of Ni^0 and $Ni^{\delta+}$ valence states as a function of annealing temperature in H_2. The full circle symbols correspond to the $Ni_xCe_{1-x}O_2$ NPs sample, while the empty circles are from reference NiO powder samples treated under identical conditions. (b) Evolution of Ce^{3+} valence state as a function of annealing temperature in H_2. The full circle symbols correspond to the $Ni_xCe_{1-x}O_2$ NPs sample, while the empty circles are from undoped CeO_2 NPs treated under identical conditions. The amount of nickel and cerium species is derived from the deconvolution of Ni $L_{3,2}$ and Ce M_5-edge sXAS spectra, respectively, and does not take into account eventual differences in the photoabsorption cross section between various oxidation states.

and dissociation of H_2 on Ni^0 [8]. The infrared characterization showed that Ce^{3+} formation might also be linked with the loss of monocoordinated hydroxyls from the surface, probably desorbed as H_2O. The ease of ceria reduction observed for $Ni_xCe_{1-x}O_2$ is consistent with several previous ab initio studies, which show that the oxygen vacancy formation energy is reduced in the case of doped-ceria as compared to the undoped one, for both substitutional [53,54,60] and interstitial [64] Ni sites.

4. Conclusions

In summary, a relatively simple and efficient approach to synthesizing undoped and Ni-doped CeO_2 nanoparticles with small particle size and size distribution is proposed. *In situ,* sXAS and DRIFT spectroscopies were used to investigate in detail the adsorbed species and the reducibility of the NPs under H_2, an important process involved in several applications of doped ceria. Ni insertion into the ceria lattice enhances the Ce^{4+} reducibility, kinetically slow over pure CeO_2, via a proposed mechanism based on electronic interaction between cerium and nickel ions at an early stage of the reduction process. The findings in this work suggest that ionic nickel is stabilized in quite harsh reducing conditions, which is an intriguing discovery calling for further investigation of their reactivity, notably in hydrogenation reactions.

CRediT author statement

Mathias Barreau: Conceptualization, Methodology, Synthesis, Investigation, Formal analysis, Writing-Original draft preparation, **Dingkai Chen**: Investigation, **Jinming Zhang**: Investigation, Visualization, **Vasiliki Papaefthimiou**: Investigation, Writing-Original draft preparation, **Corinne Petit**: Resources, **Davide Salusso**: Investigation, **Elisa Borfecchia**: Resources, Investigation, **Sylwia Turczyniak-Surdacka:** Resources, Investigation, **Kamil Sobczak**: Investigation, **Silvia Mauri**: Investigation, **Luca Braglia**: Resources, Investigation, **Piero Torelli:** Resources, Validation, **Spyridon Zafeiratos**: Conceptualization, Methodology, Writing- Original draft preparation, Visualization, Formal analysis, Supervision, Writing- Reviewing and Editing, Project administration, Funding acquisition.

Declaration of competing interest

The authors declare the following financial interests/personal relationships, which may be considered as potential competing interests: M. BARREAU reports financial support was provided by French National Research Agency.

Acknowledgment

M.B. acknowledges financial support from Strasbourg University via the IdEX-018 (Post-doctorate) project. J.Z. would like to thank the China Scholarship Council (CSC) for supporting his stay at ICPEES. D.S. and E.B. acknowledge the support from project n. 2017KKP5Z PRIN-2017 MOSCATo (Cutting-edge X-ray methods and models for the understanding of surface site reactivity in heterogeneous catalysts and sensors). We thank Dr D. Tescher for the useful and constructive discussions and S. Sall for the support with DRIFTS. We acknowledge Elettra for the allocation of synchrotron radiation beamtime and the APE-HE beamline staff for the collaboration during the experiments. This work was partially performed in the framework of the Nanoscience Foundry and Fine Analysis (NFFA-MIUR Italy Progetti Internazionali) facility. Finally, D.C. and S.Z. acknowledge the support of the French Agence Nationale de la Recherche (ANR), under contract No 236294 (project DuCaCO2).

References

[1] W. Yang, X. Wang, S. Song, H. Zhang, Syntheses and applications of noble-metal-free CeO2-based mixed-oxide nanocatalysts, Inside Chem. 5 (2019) 1743–1774, https://doi.org/10.1016/j.chempr.2019.04.009.
[2] J. Kašpar, P. Fornasiero, M. Graziani, Use of CeO2-based oxides in the three-way catalysis, Catal. Today 50 (1999) 285–298, https://doi.org/10.1016/S0920-5861(98)00510-0.

[3] F. Can, S. Berland, S. Royer, X. Courtois, D. Duprez, Composition-dependent performance of CexZr1-xO 2 mixed-oxide-supported WO3 catalysts for the NO x storage reduction-selective catalytic reduction coupled process, ACS Catal. 3 (2013) 1120−1132, https://doi.org/10.1021/cs3008329.

[4] D. Chen, D.K. Niakolas, V. Papaefthimiou, E. Ioannidou, S.G. Neophytides, S. Zafeiratos, How the surface state of nickel/gadolinium-doped ceria cathodes influences the electrochemical performance in direct CO2 electrolysis, J. Catal. 404 (2021) 518−528, https://doi.org/10.1016/j.jcat.2021.10.027.

[5] H.J. Kim, M.G. Jang, D. Shin, J.W. Han, Design of ceria catalysts for low-temperature CO oxidation, ChemCatChem 12 (2020) 11−26, https://doi.org/10.1002/cctc.201901787.

[6] J. Paier, C. Penschke, J. Sauer, Oxygen defects and surface chemistry of ceria: quantum chemical studies compared to experiment, Chem. Rev. 113 (2013) 3949−3985, https://doi.org/10.1021/cr3004949.

[7] K. Chang, H. Zhang, M.J. Cheng, Q. Lu, Application of ceria in CO2 conversion catalysis, ACS Catal. 10 (2020) 613−631, https://doi.org/10.1021/acscatal.9b03935.

[8] M. Boaro, S. Colussi, A. Trovarelli, Ceria-based materials in hydrogenation and reforming reactions for CO2 valorization, Front. Chem. (2019) 28, https://doi.org/10.3389/FCHEM.2019.00028, 0.

[9] T. Montini, M. Melchionna, M. Monai, P. Fornasiero, Fundamentals and catalytic applications of CeO2 -based materials, Chem. Rev. 116 (2016) 5987−6041, https://doi.org/10.1021/acs.chemrev.5b00603.

[10] R. Schmitt, A. Nenning, O. Kraynis, R. Korobko, A.I. Frenkel, I. Lubomirsky, S.M. Haile, J.L.M. Rupp, A review of defect structure and chemistry in ceria and its solid solutions, Chem. Soc. Rev. 49 (2020) 554−592, https://doi.org/10.1039/C9CS00588A.

[11] D.R. Mullins, The surface chemistry of cerium oxide, Surf. Sci. Rep. 70 (2015) 42−85, https://doi.org/10.1016/j.surfrep.2014.12.001.

[12] T. Sakpal, L. Lefferts, Structure-dependent activity of CeO2 supported Ru catalysts for CO2 methanation, J. Catal. 367 (2018) 171−180, https://doi.org/10.1016/j.jcat.2018.08.027.

[13] X. Liu, K. Zhou, L. Wang, B. Wang, Y. Li, Oxygen vacancy clusters promoting reducibility and activity of ceria nanorods, J. Am. Chem. Soc. 131 (2009) 3140−3141, https://doi.org/10.1021/ja808433d.

[14] A. Trovarelli, J. Llorca, Ceria catalysts at nanoscale: how do crystal shapes shape catalysis? ACS Catal. 7 (2017) 4716−4735, https://doi.org/10.1021/acscatal.7b01246.

[15] J.S. Elias, M. Risch, L. Giordano, A.N. Mansour, Y. Shao-Horn, Structure, bonding, and catalytic activity of monodisperse, transition-metal-substituted CeO2 nanoparticles, J. Am. Chem. Soc. 136 (2014) 17193−17200, https://doi.org/10.1021/ja509214d.

[16] A. Figueroba, A. Bruix, G. Kovács, K.M. Neyman, Metal-doped ceria nanoparticles: stability and redox processes, Phys. Chem. Chem. Phys. 19 (2017) 21729−21738, https://doi.org/10.1039/C7CP02820B.

[17] S. Loridant, Raman spectroscopy as a powerful tool to characterize ceria-based catalysts, Catal. Today 373 (2021) 98−111, https://doi.org/10.1016/j.cattod.2020.03.044.

[18] A.B. Kehoe, D.O. Scanlon, G.W. Watson, Role of lattice distortions in the oxygen storage capacity of divalently doped CeO2, Chem. Mater. 23 (2011) 4464−4468, https://doi.org/10.1021/cm201617d.

[19] A. Gupta, U.V. Waghmare, M.S. Hegde, Correlation of oxygen storage capacity and structural distortion in transition-metal-, noble-metal-, and rare-earth-ion-substituted CeO2 from first principles calculation, Chem. Mater. 22 (2010) 5184−5198, https://doi.org/10.1021/CM101145D.

[20] W. Shan, M. Luo, P. Ying, W. Shen, C. Li, Reduction property and catalytic activity of Ce1−XNiXO2 mixed oxide catalysts for CH4 oxidation, Appl. Catal. Gen. 246 (2003) 1−9, https://doi.org/10.1016/S0926-860X(02)00659-2.

[21] Y. Xiong, L. Li, L. Zhang, Y. Cao, S. Yu, C. Tang, L. Dong, Migration of copper species in CexCu1-xO2 catalyst driven by thermal treatment and the effect on CO oxidation, Phys. Chem. Chem. Phys. 19 (2017) 21840−21847, https://doi.org/10.1039/c7cp03735j.

[22] S. Kurajica, K. Mužina, G. Dražić, G. Matijašić, M. Duplančić, V. Mandić, M. Župančić, I.K. Munda, A comparative study of hydrothermally derived Mn, Fe, Co, Ni, Cu and Zn doped ceria nanocatalysts, Mater. Chem. Phys. 244 (2020) 122689, https://doi.org/10.1016/j.matchemphys.2020.122689.

[23] A. Figueroba, G. Kovács, A. Bruix, K.M. Neyman, Towards stable single-atom catalysts: strong binding of atomically dispersed transition metals on the surface of nanostructured ceria, Catal. Sci. Technol. 6 (2016) 6806−6813, https://doi.org/10.1039/C6CY00294C.

[24] K.J. Lee, J.H. Lee, S. Jeoung, H.R. Moon, Transformation of metal−organic frameworks/coordination polymers into functional nanostructured materials: experimental approaches based on mechanistic insights, Acc. Chem. Res. 50 (2017) 2684−2692, https://doi.org/10.1021/acs.accounts.7b00259.

[25] W. Derafa, F. Paloukis, B. Mewafy, W. Baaziz, O. Ersen, C. Petit, G. Corbel, S. Zafeiratos, Synthesis and Characterization of Nickel-Doped Ceria Nanoparticles with Improved Surface Reducibility, vol. 8, 2018, pp. 40712−40719, https://doi.org/10.1039/C8RA07995A.

[26] Y. Li, W. Han, R. Wang, L.T. Weng, A. Serrano-Lotina, M.A. Bañares, Q. Wang, K.L. Yeung, Performance of an aliovalent-substituted CoCeOx catalyst from bimetallic MOF for VOC oxidation in air, Appl. Catal. B Environ. 275 (2020) 119121, https://doi.org/10.1016/j.apcatb.2020.119121.

[27] A. Cárdenas-Arenas, A. Quindimil, A. Davó-Quiñonero, E. Bailón-García, D. Lozano-Castelló, U. De-La-Torre, B. Pereda-Ayo, J.A. González-Marcos, J.R. González-Velasco, A. Bueno-López, Design of active sites in Ni/CeO2 catalysts for the methanation of CO2: tailoring the Ni-CeO2 contact, Appl. Mater. Today 19 (2020) 100591, https://doi.org/10.1016/j.apmt.2020.100591.

[28] J. Rodríguez-Carvajal, Recent developments of the program fullprof, in: Newsl. Comm. Powder Diffr. IUCr, International Union of Crystallography, 2001, pp. 12−19.

[29] C. Castán-Guerrero, D. Krizmancic, V. Bonanni, R. Edla, A. Deluisa, F. Salvador, G. Rossi, G. Panaccione, P. Torelli, A reaction cell for ambient pressure soft x-ray absorption spectroscopy, Rev. Sci. Instrum. 89 (2018), https://doi.org/10.1063/1.5019333, 054101.

[30] E. Stavitski, F.M.F. de Groot, The CTM4XAS program for EELS and XAS spectral shape analysis of transition metal L edges, Micron 41 (2010) 687−694, https://doi.org/10.1016/j.micron.2010.06.005.

[31] S.K. Misra, S.I. Andronenko, M.H. Engelhard, A. Thurber, K.M. Reddy, A. Punnoose, Role of dopant incorporation on the magnetic properties of Ce1−xNixO2 nanoparticles: an electron paramagnetic resonance study, J. Appl. Phys. 103 (2008), https://doi.org/10.1063/1.2833291, 07D122.

[32] D.-K. Lim, N.W. Kwak, J.-S. Kim, H. Kim, B.-K. Kim, Y.-C. Kim, W. Jung, Ni diffusion in ceria lattice: a combined experimental and theoretical study, Acta Mater. 219 (2021) 117252, https://doi.org/10.1016/j.actamat.2021.117252.

[33] Z. Chafi, N. Keghouche, C. Minot, DFT study of Ni−CeO2 interaction: adsorption and insertion, Surf. Sci. 601 (2007) 2323−2329, https://doi.org/10.1016/j.susc.2007.03.041.

[34] D. Schweke, Y. Mordehovitz, M. Halabi, L. Shelly, S. Hayun, Defect chemistry of oxides for energy applications, Adv. Mater. 30 (2018) 1706300, https://doi.org/10.1002/adma.201706300.

[35] J.E. Spanier, R.D. Robinson, F. Zhang, S.-W. Chan, I.P. Herman, Size-dependent properties of CeO2-y nanoparticles as studied by Raman scattering, Phys. Rev. B 64 (2001) 245407, https://doi.org/10.1103/PhysRevB.64.245407.

[36] C. Schilling, A. Hofmann, C. Hess, M.V. Ganduglia-Pirovano, Raman spectra of polycrystalline CeO2: a density functional theory study, J. Phys. Chem. C 121 (2017) 20834−20849, https://doi.org/10.1021/acs.jpcc.7b06643.

[37] S. Mahammadunnisa, P. Manoj Kumar Reddy, N. Lingaiah, C. Subrahmanyam, NiO/Ce1-xNixO2-δ as an alternative to noble metal catalysts for CO oxidation, Catal. Sci. Technol. 3 (2013) 730−736, https://doi.org/10.1039/c2cy20641b.

[38] C.A. Chagas, E.F. de Souza, R.L. Manfro, S.M. Landi, M.M.V.M. Souza, M. Schmal, Copper as promoter of the NiO-CeO2 catalyst in the preferential CO oxidation, Appl. Catal. B Environ. 182 (2016) 257−265, https://doi.org/10.1016/j.apcatb.2015.09.033.

[39] G.M. Mullen, E.J. Evans, B.C. Siegert, N.R. Miller, B.K. Rosselet, I. Sabzevari, A. Brush, Z. Duan, C. Buddie Mullins, The interplay between ceria particle size, reducibility, and ethanol oxidation activity of ceria-supported gold catalysts, React. Chem. Eng. 3 (2018) 75−85, https://doi.org/10.1039/C7RE00175D.

[40] J.P. Holgado, R. Alvarez, G. Munuera, Study of CeO2 XPS spectra by factor analysis: reduction of CeO2, Appl. Surf. Sci. 161 (2000) 301−315, https://doi.org/10.1016/S0169-4332(99)00577-2.

[41] F. Giordano, A. Trovarelli, C. De Leitenburg, M. Giona, A model for the temperature-programmed reduction of low and high surface area ceria, J. Catal. 193 (2000) 273−282, https://doi.org/10.1006/jcat.2000.2900.

[42] C.W. Hu, J. Yao, H.Q. Yang, Y. Chen, A.M. Tian, On the inhomogeneity of low nickel loading methanation catalyst, J. Catal. 166 (1997) 1−7, https://doi.org/10.1006/jcat.1997.1469.

[43] C. Binet, M. Daturi, J.C. Lavalley, IR study of polycrystalline ceria properties in oxidised and reduced states, Catal. Today 50 (1999) 207−225, https://doi.org/10.1016/S0920-5861(98)00504-5.

[44] O. Pozdnyakova, D. Teschner, A. Wootsch, J. Kröhnert, B. Steinhauer, H. Sauer, L. Toth, F.C. Jentoft, A. Knop-Gericke, Z. Paál, R. Schlögl, Preferential CO oxidation in hydrogen (PROX) on ceria-supported catalysts, part I: oxidation state and surface species on Pt/CeO2 under reaction conditions, J. Catal. 237 (2006) 1−16, https://doi.org/10.1016/j.jcat.2005.10.014.

[45] A. Badri, C. Binet, J.C. Lavalley, An FTIR study of surface ceria hydroxy groups during a redox process with H2, J. Chem. Soc. - Faraday Trans. 92 (1996) 4669−4673, https://doi.org/10.1039/ft9969204669.

[46] B. Sudduth, D. Yun, J. Sun, Y. Wang, Facet-Dependent selectivity of CeO2 nanoparticles in 2-Propanol conversion, J. Catal. 404 (2021) 96−108, https://doi.org/10.1016/j.jcat.2021.09.009.

[47] C. Binet, A. Badri, J.-C. Lavalley, A spectroscopic characterization of the reduction of ceria from electronic transitions of intrinsic point defects, J. Phys. Chem. 98 (1994) 6392−6398.

[48] A. Ruosi, C. Raisch, A. Verna, R. Werner, B.A. Davidson, J. Fujii, R. Kleiner, D. Koelle, Electron sampling depth and saturation effects in perovskite films investigated by soft x-ray absorption spectroscopy, Phys. Rev. B 90 (2014) 125120, https://doi.org/10.1103/PhysRevB.90.125120.

[49] W. Gu, H. Wang, K. Wang, Nickel L-edge and K-edge X-ray absorption spectroscopy of non-innocent Ni[S2C2(CF3)2]2n series (n = −2{,} −1{,} 0): direct probe of nickel fractional oxidation state changes, Dalt. Trans. 43 (2014) 6406−6413, https://doi.org/10.1039/C4DT00308J.

[50] H. Wang, D.S. Patil, W. Gu, L. Jacquamet, S. Friedrich, T. Funk, S.P. Cramer, L-edge X-ray absorption spectroscopy of some Ni enzymes: probe of Ni

electronic structure, J. Electron Spectros. Relat. Phenomena 114–116 (2001) 855–863, https://doi.org/10.1016/S0368-2048(00)00370-4.
[51] M. Al Samarai, A.W. Hahn, A. Beheshti Askari, Y.T. Cui, K. Yamazoe, J. Miyawaki, Y. Harada, O. Rüdiger, S. Debeer, Elucidation of structure-activity correlations in a nickel manganese oxide oxygen evolution reaction catalyst by operando Ni L-edge X-ray absorption spectroscopy and 2p3d resonant inelastic X-ray scattering, ACS Appl. Mater. Interfaces 11 (2019) 38595–38605, https://doi.org/10.1021/acsami.9b06752.
[52] H. Wang, S.M. Butorin, A.T. Young, J. Guo, Nickel oxidation states and spin states of bioinorganic complexes from nickel L-edge X-ray absorption and resonant inelastic X-ray scattering, J. Phys. Chem. C 117 (2013) 24767–24772, https://doi.org/10.1021/jp402404b.
[53] W. Zhang, M. Pu, M. Lei, Theoretical studies on the stability and reactivity of the metal-doped CeO2(100) surface: toward H2 dissociation and oxygen vacancy formation, Langmuir 36 (2020) 5891–5901, https://doi.org/10.1021/acs.langmuir.0c00644.
[54] W.Q. Li, S. Goverapet Srinivasan, D.R. Salahub, T. Heine, Ni on the CeO2(110) and (100) surfaces: adsorption vs. substitution effects on the electronic and geometric structures and oxygen vacancies, Phys. Chem. Chem. Phys. 18 (2016) 11139–11149, https://doi.org/10.1039/C6CP00738D.
[55] F. De Groot, Multiplet effects in X-ray spectroscopy, Coord. Chem. Rev. 249 (2005) 31–63, https://doi.org/10.1016/j.ccr.2004.03.018.
[56] X. Zheng, B. Zhang, P. De Luna, Y. Liang, R. Comin, O. Voznyy, L. Han, F.P. García de Arquer, M. Liu, C.T. Dinh, T. Regier, J.J. Dynes, S. He, H.L. Xin, H. Peng, D. Prendergast, X. Du, E.H. Sargent, Theory-driven design of high-valence metal sites for water oxidation confirmed using in situ soft X-ray absorption, Nat. Chem. 10 (2018) 149–154, https://doi.org/10.1038/nchem.2886.
[57] G. van der Laan, B.T. Thole, G.A. Sawatzky, M. Verdaguer, Multiplet structure in the L2,3 X-ray-absorption spectra: a fingerprint for high- and low-spin Ni2+ compounds, Phys. Rev. B 37 (1988) 6587–6589, https://doi.org/10.1103/PhysRevB.37.6587.
[58] R.J.O. Mossanek, G. Domínguez-Cañizares, A. Gutiérrez, M. Abbate, D. Díaz-Fernández, L. Soriano, Effects of Ni vacancies and crystallite size on the O 1s and Ni 2p x-ray absorption spectra of nanocrystalline NiO, J. Phys. Condens. Matter 25 (2013) 495506, https://doi.org/10.1088/0953-8984/25/49/495506.
[59] G.I. Svirskiy, A. V Generalov, N.A. Vinogradov, X.O. Brykalova, A. V Vereshchagin, O. V Levin, A.G. Lyalin, A.B. Preobrajenski, A.S. Vinogradov, Electronic structure of the [Ni(Salen)] complex studied by core-level spectroscopies, Phys. Chem. Chem. Phys. 23 (2021) 11015–11027, https://doi.org/10.1039/D1CP00511A.
[60] Y.-Q. Su, L. Zhang, V. Muravev, E.J.M. Hensen, Lattice oxygen activation in transition metal doped ceria, Chinese J. Catal. 41 (2020) 977–984, https://doi.org/10.1016/S1872-2067(19)63468-6.
[61] L. Zhong, M. Barreau, V. Caps, V. Papaefthimiou, M. Haevecker, D. Teschner, W. Baaziz, E. Borfecchia, L. Braglia, S. Zafeiratos, Improving the catalytic performance of cobalt for CO preferential oxidation by stabilizing the active phase through vanadium promotion, ACS Catal. 11 (2021) 5369–5385, https://doi.org/10.1021/acscatal.0c05482.
[62] Z. Mao, P.G. Lustemberg, J.R. Rumptz, M.V. Ganduglia-Pirovano, C.T. Campbell, Ni nanoparticles on CeO2(111): energetics, electron transfer, and structure by Ni adsorption calorimetry, spectroscopies, and density functional theory, ACS Catal. 10 (2020) 5101–5114, https://doi.org/10.1021/acscatal.0c00333.
[63] C. Lamonier, A. Ponchel, A. D'Huysser, L. Jalowiecki-Duhamel, Studies of the cerium-metal-oxygen-hydrogen system (metal=Cu, Ni), Catal. Today 50 (1999) 247–259, https://doi.org/10.1016/S0920-5861(98)00507-0.
[64] X. Wang, M. Shen, J. Wang, S. Fabris, Enhanced oxygen buffering by substitutional and interstitial Ni point defects in ceria: a first-principles DFT+U study, J. Phys. Chem. C 114 (2010) 10221–10228, https://doi.org/10.1021/jp101100f.